

Topology Optimization of the Caudal Fin of the Three-Dimensional Self-Propelled Swimming Fish

Zhiqiang Xin¹ and Chuijie Wu^{1,2,*}

¹ College of Mechanics and Materials, Hohai University, Nanjing 210098, China

² State Key Laboratory of Structural Analysis for Industrial Equipment & School of Aeronautics and Astronautics, Dalian University of Technology, Dalian 116024, China

Received 3 November 2013; Accepted (in revised version) 30 April 2014

Available online 7 August 2014

Abstract. Based on the boundary vorticity-flux theory, topology optimization of the caudal fin of the three-dimensional self-propelled swimming fish is investigated by combining unsteady computational fluid dynamics with moving boundary and topology optimization algorithms in this study. The objective functional of topology optimization is the function of swimming efficiency, swimming speed and motion direction control. The optimal caudal fin, whose topology is different from that of the natural fish caudal fin, make the 3D bionic fish achieve higher swimming efficiency, faster swimming speed and better maneuverability. The boundary vorticity-flux on the body surface of the 3D fish before and after optimization reveals the mechanism of high performance swimming of the topology optimization bionic fish. The comparative analysis between the swimming performance of the 3D topology optimization bionic fish and the 3D lunate tail bionic fish is also carried out, and the wake structures of two types of bionic fish show the physical nature that the swimming performance of the 3D topology optimization bionic fish is significantly better than the 3D lunate tail bionic fish.

AMS subject classifications: 76Z10, 74F10

Key words: 3D bionic fish, caudal fin, topology optimization, swimming performance, vortex dynamics.

1 Introduction

Through hundreds of millions of years of natural evolution, most fishes achieve excellent swimming performance, which the motion performance of man-made vehicles can not catch up with. So the secret of fish swimming attracts interests and exploring of

*Corresponding author.

Email: cjwudut@dlut.edu.cn (C. J. Wu)

researchers from all areas. Gray estimated that the muscle energy of a dolphin at a swimming speed between 15 and 20 knots is one-seventh of the energy needed to drag a rigid body at the same speed [1]. The results of the study are known as the famous Gray's paradox, which promotes the study of fish swimming into a peak. From then on many researchers explain or challenge the conclusions of Gray's paradox. Lighthill studied anguilliform and carangiform swimming using the elongated-body theory. Wu proposed a two-dimensional waving plate theory for fish swimming [2]. However, these analytical methods can be only employed to calculate the thrust and the lateral forces of a undulating plates or a pitch-heave wing and have significant limitations in modeling realistic fish swimming. Cheng [3] developed a semi-numerical and semi-analytical method to analyze the propulsion mechanism of a 3D waving plate. Candelier et al. extended Lighthill's large-amplitude elongated-body theory of the fish locomotion to the three-dimensional movements, and founded that the results predicted with the three-dimensional extension theory are in good agreement with the data obtained in the numerical simulations [4].

Fish swimming is a unsteady flow process, and the swimming performance and features are closely related to wake structure generated in fish swimming. Fish can efficiently take advantage of the mechanism of unsteady flow. In order to reveal the efficient swimming mechanism of fish, it is necessary to analyze clearly the three-dimensional flow field around the swimming fish body using the advanced experimental techniques and numerical simulation methods. The experimental studies of fish swimming have made many important progress, for example, Lauder et al. [5,6] performed a large number of experiments of fish swimming, and systematically analyzed how different fishes use body and appendages to effectively implement flow control both actively and passively. Triantafyllou et al. [7,8] studied the relationship between the propulsive efficiency and the Strouhal number, and described the wake characteristics corresponding to the optimum propulsive efficiency. Due to the enormous difficulties in controlling fish swimming in the experiment, the numerical simulation is more effective in comparison with the experiment. The impact of various physical parameters and swimming patterns on the swimming mechanism, even evolutionary process and the geometry optimization of fish, can be carried out in the numerical simulation. Anderson and Wolfgang et al. shown the generation of the vortex around the fish body and the wake vorticity control during fish turning maneuver. Liu et al. [9] simulated tadpoles swimming by CFD, and analyzed the process of vortex shedding in the undulatory swimming. Wu and Wang [10] implemented numerical simulations of self-propelled swimming of the 3D bionic fish school based on the three-dimensional Navier-Stokes equations, and founded that fish control the swimming direction mainly by the swing of the head.

Fish are very diverse in the nature, and various types of fish have different shapes and swimming maneuvers. Generally, swimming locomotion can be divided into periodic swimming at a almost constant speed and transient movements, such as rapid maneuvers and turn etc. According to the swimming propulsors of fish, swimming modes are classified into the body and/or caudal fin swimming (BCF) and median and paired fin

swimming (MPF). About 15% of the fishes employ MPF modes as the routine swimming means, while most fishes use BCF modes to generate the thrust [11]. Thus the caudal fin plays a key role in the fish locomotion. Most of the thrust is provided by the caudal fin for tuna and other large fishes. However, not many studies of shape and function of the fish tail are performed. Using digital particle image velocimetry (DPIV) flow visualization data, the vortex structure and force balance of two types of fishes with the heterocercal and homocercal tail during steady swimming are comparatively analyzed, and the characteristics of morphology and function of the two types of the tail are described [12]. Lauder [13] found that scomber japonicus and other fishes use the symmetrical fork tail fin to achieve efficient swimming. Heo et al. [14] found that the tail with a distributed thickness makes the bionic robotic fish swim faster and save more energy. Compared with whales and dolphins, the tail fin of tuna has a higher swimming efficiency [15].

It is actually a process of flow control, that a variety of fishes employ the tails with different morphologies for propulsion. The optimal flow control has already attracted the interests of the majority of researchers, due to its great application value. Great progress is made in the shape optimization, and the biggest demand is for the wing shape optimization, which always aims at smaller resistance and the largest lift. However, the shape optimization can only change the shape of the boundary given in initial design. The topology optimization methods in solid mechanics can be applied to flow problem to overcome this limitation. The topology optimization can produce complex and non-intuition optimal structure. The initial geometry is not necessarily close to the optimal geometry. Bendsøe Sigmund [16] detail the main concepts of the topology optimization.

The topology optimization goal is to find the optimal topology in the feasible region, which makes objective function reach the maximum or minimum. While the topology optimization has achieved considerable development in the structural optimization, the topology optimization of fluid problems is just in the exploration stage. Borrvall and Petersson [17] varied the distribution of porous materials by changing Darcy permeability tensor in the topology optimization of the Stokes flow. Guest and Prevest [18] developed a Darcy-Stokes finite element method to solve the topology optimization of creeping fluid flows. Distinguished from the previous literature, there are only two extreme cases, the pure solid and fluid, in the optimization domain. It can be seen that the methods in two articles are just for Stokes flow problems. Olesen and Okkels [19] studied the topology optimization problem of the steady Navier-Stokes flow. Zhou and Li [20] demonstrated a variational level set method for the topology optimization of steady Navier-Stokes flow, and shown several 2D and 3D examples using this method. Duan and Ma [21] developed a topology optimization algorithm method, which is also based on the variational level set method, but can handle the Navier-Stokes flow problem.

The topology optimization of the caudal fin of the three-dimensional self-propelled swimming bionic fish in the unsteady Navier-Stokes flow is carried out in the present study. The adaptive mesh refinement method, the immersed boundary method and the volume of fluid (VOF) method are used to portray the moving boundary of the three-dimensional self-propelled swimming bionic fish. The caudal fin is assumed to a perme-

able region, in which the water permeability is a coefficient varying between 0 and 1. The water permeability of the fish body and the fluid are two extreme cases, corresponding to 0 and 1, respectively. Based on the boundary vorticity-flux (BVF) theory [22, 23], the underlying fluid physical sources can be traced to the moving body surface, where all the vorticity is generated in fish swimming. The distributions and variations of the BVF on the fish body before and after the topology optimization are studied, and the comparative analysis of the swimming performance and the 3D vortex structures of the 3D topology optimization bionic fish and the lunatae tail fish are also investigated in the present study.

2 Computational fluid dynamics numerical algorithm with the moving boundary

2.1 Governing equations and numerical algorithm

The governing equations for the fluid flow systems are the incompressible continuity equation and 3D unsteady Navier-Stokes equations defined by

$$\nabla \cdot \mathbf{u} = 0, \quad (2.1a)$$

$$\frac{\partial \mathbf{u}}{\partial t} + (\mathbf{u} \cdot \nabla) \mathbf{u} = -\nabla \left(\frac{p}{\rho} + gz \right) + \nu \nabla^2 \mathbf{u}, \quad (2.1b)$$

where \mathbf{u} , p , ρ , g and $\nu = \mu/\rho$ are fluid velocity, pressure, density, gravity acceleration and kinematic viscosity, respectively. μ is dynamic viscosity.

The finite volume method is employed to solve the unsteady Navier-Stokes equations. The Poisson equation of pressure is solved using the projection method and the multi-grid method. The second-order Godunov type scheme is used to discretize the convection terms. The diffusion terms are discretized with the implicit Crank-Nicolson scheme that removes the viscous stability constraint. The fractional-step projection method is employed for integrating the equations in time. Computational domains are discretized using the adaptive multi-grid finite volumes. In the self-propelled swimming of the 3D bionic fish, the fish body boundaries are treated with the immersed boundary method and the volume of fluid (VOF) method. The vorticity and ∇Tr are together used as adaptive refinement criteria, where Tr is the tracking scalar of VOF (Volume of Fluid). The foregoing methods are described in detail as follow, according to [10].

The temporal discretization is handled with the fractional-step projection method. For any given time step n , the fluid velocity \mathbf{u}^n and the fractional-step pressure $\nabla p^{n-1/2}$ are all known. The temporary velocity field \mathbf{u}^{**} is obtained by using

$$\frac{\mathbf{u}^{**} - \mathbf{u}^n}{\Delta t} + \nabla p^{n-1/2} = [-(\mathbf{u} \cdot \nabla) \mathbf{u}]^{n+1/2} + \frac{\nu}{2} \nabla^2 (\mathbf{u}^{**} + \mathbf{u}^n). \quad (2.2)$$

The new velocity field \mathbf{u}^{n+1} and the fractional-step pressure field $p^{n+1/2}$ are then yielded by applying a projection operator to \mathbf{u}^{**} . This projection method depends on the the

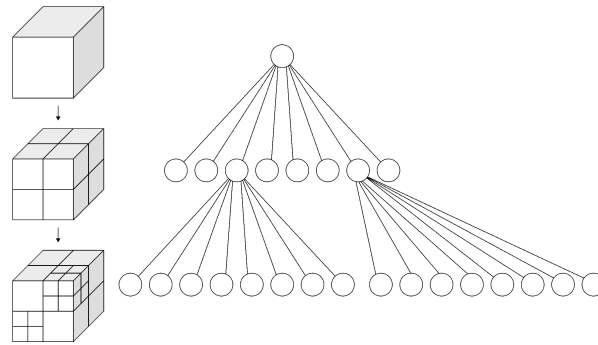


Figure 1: Example of octree discretization and its corresponding tree representation.

Hodge decomposition of the velocity field, i.e.,

$$\mathbf{u}^{**} = \mathbf{u}^{n+1} + \Delta\phi^{n+1}, \quad (2.3)$$

where \mathbf{u} satisfies $\nabla \cdot \mathbf{u}^{n+1} = 0$ in the computational domain Ω , and $\mathbf{u}^{n+1} \cdot \mathbf{n} = 0$ on $\partial\Omega$. $\partial\Omega$ is the boundary of the computational domain Ω . The following Poisson equation is obtained by taking the divergence of two sides of Eq. (2.3),

$$\nabla^2 \phi^{n+1} = \frac{1}{\Delta t} \nabla \cdot \mathbf{u}^{**}, \quad (2.4)$$

with the boundary condition

$$\frac{\partial \phi}{\partial \mathbf{n}} = 0 \quad \text{on } \partial\Omega, \quad (2.5)$$

where \mathbf{n} is the unit normal vector to the boundaries. Thus, the divergence-free velocity field can be defined as

$$\mathbf{u}^{n+1} = \mathbf{u}^{**} - \Delta t \phi^{n+1}, \quad (2.6)$$

where ϕ^{n+1} is obtained by solving the Poisson equation (2.4). Eq. (2.6) defines the projection from the \mathbf{u}^{**} to the divergence-free velocity field \mathbf{u} . The new fractional step pressure is given as

$$p^{n+1/2} = p^{n-1/2} + \phi^{n+1}. \quad (2.7)$$

The computational domain is spatially discretized with cubic finite volumes organized hierarchically as an octree, as shown in Fig. 1. In the following, each finite volume is referred to as a *cell*. Each cell may be the *parent* cell of eight *children* cells. *Root cell* is the base of the tree structure, and *leaf cell* has not children cells. Each initial cube can be divided into eight smaller cubes. Splitting each cube can be done iteratively to meet the required refinement. Thus, the total number of cells becomes 8^n after the n th refinement.

2.2 Adaptive moving boundaries with the Ghost-cell immersed boundary method

In the present study, the boundaries of the self-propelled swimming fish body are treated with ghost-cell immersed boundary method (IBM), which employs discrete forcing where the forcing is directly applied to the discretized Navier-Stokes equations. Ghost cell is the cell located inside the solid, which has at least one adjacent cell in the fluid. When the immersed boundaries are determined, the entire computational region is divided into two parts, namely, the fluid domain and the Ghost cell domain, as shown in Fig. 2(a). The values of flow variables at the Ghost cells are extrapolated from the information of nearby fluid points and associated solid boundaries.

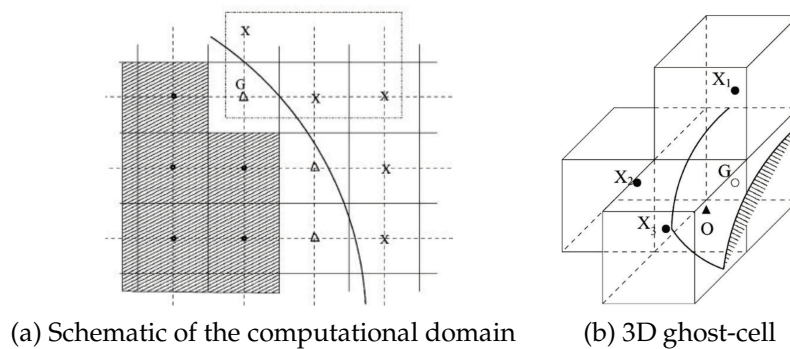


Figure 2: Schematics of the computational domain with an immersed boundary. (a) X represent points in the flow region, the shaded domain represents solid region and G is ghost cell. (b) x_1, x_2, x_3 are points in the fluid domain, O is point on the immersed boundary, G is ghost cell.

For a variable ϕ , the linear interpolation in 3D,

$$\phi = a_0 + a_1x + a_2y + a_3z. \tag{2.8}$$

The coefficients can be computed using the values of the variables of three nearest point (x_1, x_2, x_3) from the ghost cell in the fluid domain and O point on the immersed boundary, as shown in Fig. 2(b)

$$A = B^{-1}\Phi, \tag{2.9}$$

where

$$B = \begin{bmatrix} 1 & x_0 & y_0 & z_0 \\ 1 & x_1 & y_1 & z_1 \\ 1 & x_2 & y_2 & z_2 \\ 1 & x_3 & y_3 & z_3 \end{bmatrix}. \tag{2.10}$$

The linear interpolation has only first-order accuracy. For the second-order accuracy, the quadratic reconstruction can be used,

$$\phi = a_0 + a_1x + a_2y + a_3z + a_4x^2 + a_5xy + a_6xz + a_7yz + a_8y^2 + a_9z^2. \tag{2.11}$$

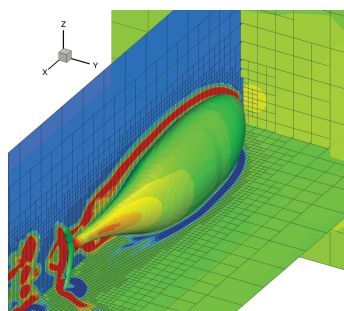


Figure 3: The 3D self-propelled swimming fish immersed in the adaptive meshes.

Accordingly, nine neighbor points are required in the interpolation. Considering the computation time and accuracy together, the linear interpolation is used in the present study, while the adaptive refinement method is employed to enhance the resolution of the immersed boundaries.

The realization of the adaptive refinement method is constituted of two steps. First of all, all the leaf cells that satisfy a refinement criterion are refined. Secondly, the parent cells, of which all leaf cells do not satisfy the given criterion, are coarsened. In order to ensure that meshes intersecting with moving body boundaries is always the finest grids, the adaptive refinement criteria are based on both vorticity and ∇Tr , where Tr is a tracer of VOF. Then the combinational refinement conditions of grids are

$$\max\left(\frac{h\|\nabla Tr\|}{\max\|Tr\|}, \frac{h\|\nabla \times \mathbf{u}\|}{\max\|\mathbf{u}\|}\right) > \tau, \quad (2.12)$$

where h is the minimum width of meshes, and $0 < \tau < 1$ is the threshold value of adaptive refinement. If the region surrounded by the moving boundary is Ω , then

$$Tr \begin{cases} = 0 & \text{in } \Omega, \\ \in (0,1) & \text{on } \partial\Omega, \\ = 1 & \text{outside } \Omega. \end{cases} \quad (2.13)$$

In each cell, the following three cases exist:

- (1) $Tr = 1$, when the cell was completely full of fluid;
- (2) $Tr = 0$, when the cell was completely full of solid;
- (3) $0 < Tr < 1$, when the fluid-solid interface cuts the cell.

Fig. 3 is the local computation domain around the 3D self-propelled swimming fish immersed in the adaptive meshes, of which the refinement criteria are the vorticity and ∇Tr . In Fig. 3, the (x, y) plane, the (x, z) plane, the (y, z) plane and fish body are colored by the distribution of ω_z , vorticity ω and the pressure, respectively.

2.3 Validation cases

To verify the above adaptive grid algorithm described in the previous two sections, the simulations of the three-dimensional flow around a sphere and the three-dimensional flow around an oscillating foil in an unbounded uniform flow field are performed, respectively. In this study, all calculations are performed using dimensionless quantities.

2.3.1 Flow around a sphere

The computational domain is $32D \times 8D \times 8D$ (*length* \times *width* \times *height*, D is the diameter of the sphere). The initial fluid velocity is $u_\infty = 1.00$, and Reynolds number is $Re_D = 100$ ($Re_D = u_\infty D / \nu$). Fig. 5 shows the drag coefficient computed in two case, in which the sizes of the minimum mesh are $0.125D$ and $0.0625D$. Namely, the finest levels of adaptive mesh refinement are taken as 6 and 7, respectively. The corresponding values of the drag coefficient are 1.029 and 1.087, respectively. The values, especially obtained in the finest grid, are in good agreement with the results ($C_D = 1.1$) of the experiment [24] in the same conditions. Fig. 4 represents the vorticity field in the wake of the flow passing the sphere at $Re_D = 100$. Fig. 6 shows the streamlines in this case. It can be seen from the two figures that the wake is axisymmetric and steady, and the size and strength of the vortex in the rear of the sphere are also in good agreement with the previous work. This shows that the the adaptive refinement method with the Ghost-cell immersed boundary used in the present study is efficient and reliable.

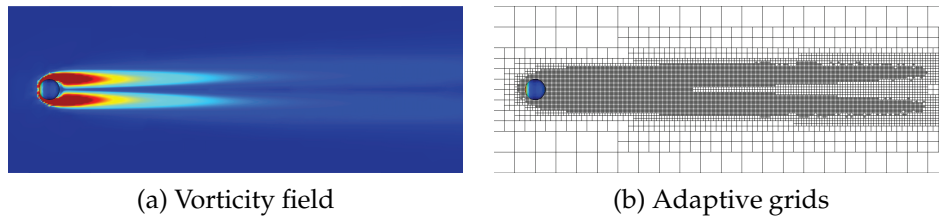


Figure 4: The vorticity contours and the corresponding adaptive grids of the flow past the sphere at $Re_D = 100$.

2.3.2 Flow around around an oscillating foil

The computational domain is $12c \times 8c \times 4c$ (*length* \times *width* \times *height*, c is the length of the chord). The oscillating foil takes the shape of NACA 0012 in chord-wise sections. The oscillating foil perform a heave motion $h(t)$ and a pitch motion $\theta_f(t)$. The pitch motion has a phase difference ψ_f with the heave motion. The specific oscillating rule is defined by

$$\begin{cases} h(t) = h_0 \sin(\omega_f t), \\ \theta_f(t) = \theta_0 \sin(\omega_f t + \psi_f), \end{cases} \quad (2.14)$$

where h_0 is the amplitude of the heave motion, θ_0 is the amplitude of the pitch motion, and ω_f is the frequency of the oscillating motion.

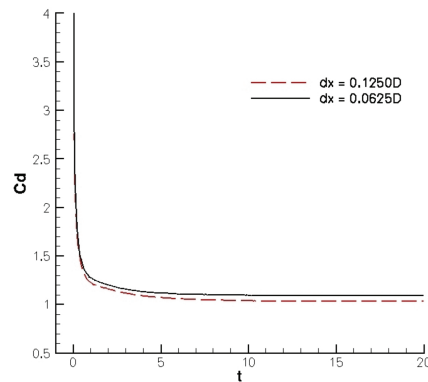


Figure 5: The drag coefficients of the sphere at $Re_D = 100$.

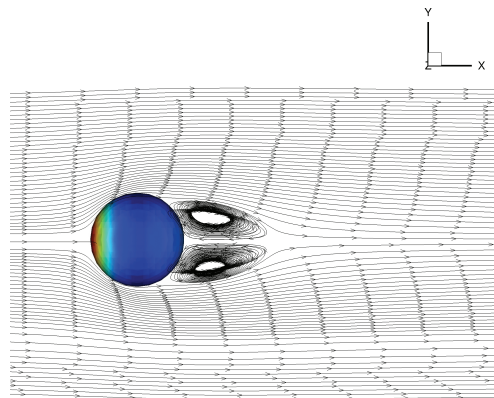


Figure 6: The axisymmetric streamlines past the sphere at $Re_D = 100$.

The initial fluid velocity is $u_\infty = 1.00$, and Reynolds number is $Re_c = 40000$ ($Re_c = u_\infty c / \nu$). The simulations are performed for different Strouhal numbers ($St_f = \omega_f h_0 / \nu \pi$) 0.1, 0.2, 0.3, 0.4 and 0.5. For each Strouhal number, the heave amplitude, the pitch amplitude, and the relative phase angle are taking values of $h_0/c = 0.75$, $\theta_0 = 30^\circ$ and $\psi_f = 90^\circ$, respectively. The results of the present CFD simulations are compared with the experimental values given by Anderson [25]. The thrust coefficient is defined as

$$C_T = \frac{F_T}{\frac{1}{2} \rho U_\infty^2 S_0}, \quad (2.15)$$

where F_T is the thrust, $S_0 = sc$ is the area of the foil, and s denotes the span. Fig. 7 shows that the values of our numerical simulations are in good agreement with the results of the [25]. It can be seen from Fig. 8 that the meshes around the surface of the oscillation foil and in the region with high vorticity are the finest.

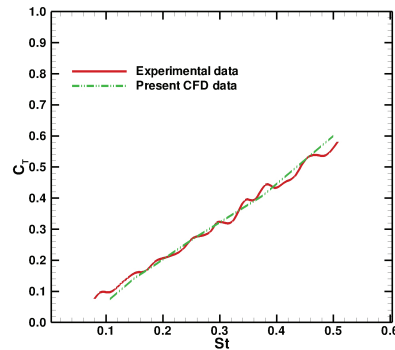


Figure 7: Thrust coefficient C_T .

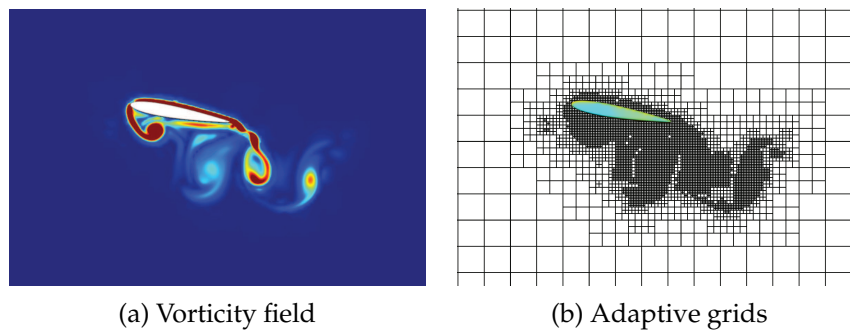


Figure 8: The vorticity contours and the corresponding adaptive grids of the flow around an oscillating foil.

3 Motion equations and swing parameters of a 3D bionic fish

3.1 The geometry of three-dimensional bionic fish

In the study of self-propelled swimming of the three-dimensional bionic fish, two sets of coordinates are used, as shown in Fig. 9, namely, the global coordinates (x, y, z) and the local coordinates (x_l, y_l, z_l) , also called as the fish body coordinate that is settled on the centre of the mass of the fish body. The global coordinates and fish body coordinates can be converted to each other. The geometry of the three-dimensional tuna given by Wu [10] is used in the present study. The fish body mainly consists of two parts, namely, the body trunk and the lunate caudal fin. The profile of the three-dimensional bionic fish is defined by

$$\begin{cases} z_l(x_l) = \pm 0.152 \tanh(6x_l + 1.8), & -0.3 \leq x_l \leq 0.1, \\ z_l(x_l) = \pm [0.075 - 0.076 \tanh(7x_l - 3.15)], & 0.1 < x_l \leq 0.35, \\ z_l(x_l) = \pm [1.749 \tanh(x_l) - 3.331 \tanh(2x_l) + 1.976 \tanh(3x_l)], & 0.35 < x_l \leq 0.7. \end{cases} \quad (3.1)$$

At each horizontal position x_l , the body cross-sections are ellipses with a major to minor ratio, which equals 1.5. The leading edge and trailing edge profile of the lunate caudal

fin are defined by

$$\begin{cases} x_l(z_l)_{LE} = 39.543|z_l|^3 - 3.685(z_l)^2 + 0.636|z_l| + 0.7, & -0.15 \leq z_l \leq 0.15, \\ x_l(z_l)_{TE} = -40.74|z_l|^3 + 9.666(z_l)^2 + 0.77, & -0.15 \leq z_l \leq 0.15. \end{cases} \quad (3.2)$$

Where LE and TE indicate the leading edge and trailing edge, respectively. The caudal fin takes the shape of NACA 0040 in chord-wise sections. The profile and geometry of the three-dimensional bionic fish are shown in Fig. 10 and Fig. 11. In the present study, the finest level of adaptive mesh refinement is 7. Thus the minimum height of the chord-wise section of the caudal fin is 1.2 times larger than the width of the finest grid, with the method of adaptive multi-grids. The body and caudal fin of the 3D bionic fish can be distinguished by the immersed boundary method, as shown in Fig. 3.

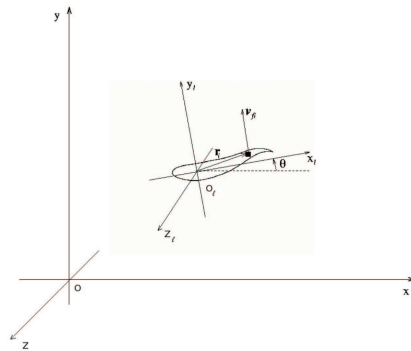


Figure 9: The local coordinate and the global coordinate.

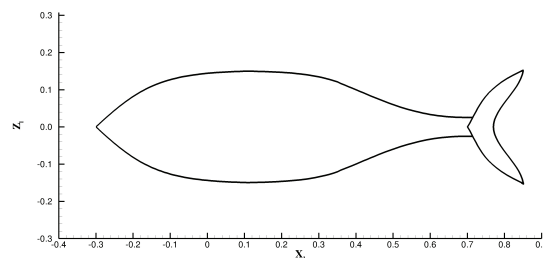


Figure 10: The profile of the 3D bionic fish.

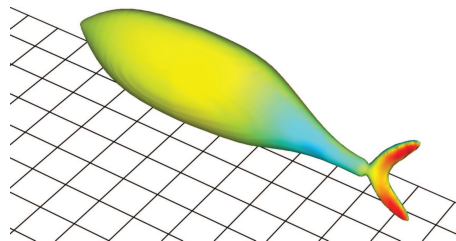


Figure 11: The geometry of the 3D bionic fish.

3.2 Dynamics equations

The dynamics equations for the 3D self-propelled swimming fish are

$$m \frac{d\mathbf{u}}{dt} = \mathbf{F}, \quad \frac{d\mathbf{L}}{dt} = \mathbf{M}, \tag{3.3}$$

where m is the mass of the 3D bionic fish; \mathbf{u} is the velocity vector; \mathbf{F} is the hydrodynamic force; \mathbf{M} is the moment and \mathbf{L} is the moment of momentum. The hydrodynamic force and moment exerted on fish body are given as

$$\mathbf{F} = - \int_{\partial B} (-p\mathbf{n} + \mu\boldsymbol{\omega} \times \mathbf{n}) ds, \tag{3.4a}$$

$$\mathbf{M} = - \int_{\partial B} \mathbf{x} \times (-p\mathbf{n} + \mu\boldsymbol{\omega} \times \mathbf{n}) ds + \mathbf{M}_{sB}, \tag{3.4b}$$

$$\mathbf{F} = - \int_{\partial B} \rho \mathbf{x} (1/2\sigma_p + \sigma_{vis}) ds, \tag{3.4c}$$

$$\mathbf{M} = - \int_{\partial B} \rho [1/2x^2(\sigma_p + \sigma_{vis}) - \mathbf{x}\mathbf{x} \cdot \sigma_{vis}] ds + \mathbf{M}_{sB}, \tag{3.4d}$$

where Eq. (3.4a) and Eq. (3.4b) are force and moment expressions derived directly from the momentum balance, respectively. Eq. (3.4c) and Eq. (3.4d) are force and moment formulas based on the boundary vorticity flux, respectively [22, 23]. ∂B is the surface of the 3D bionic fish body, \mathbf{n} is the unit outward-pointing normal vector of fish body surface; ρ , μ , $\boldsymbol{\omega}$ are fluid density, dynamic viscosity and vorticity, respectively; $\sigma_p = \mathbf{n} \times \nabla p / \rho$, $\sigma_{vis} = \nu(\mathbf{n} \times \nabla) \times \boldsymbol{\omega}$ are the boundary vorticity flux components caused by the tangential pressure gradient and the viscous vortical effect, respectively. $\mathbf{M}_{sB} = -2\mu \int_B \boldsymbol{\omega}_B dV$, where $\boldsymbol{\omega}_B$ is angular speed of the fish body.

The moment of momentum is defined by

$$\mathbf{L} = \sum_i m_i \mathbf{r}_i \times \mathbf{v}_i, \tag{3.5}$$

where m_i is the mass of segment i on fish body, \mathbf{r}_i is the position vector of the gravity center of segment i in the local coordinates, as shown in Fig. 9. \mathbf{v}_i is the velocity segment i , and include two parts,

$$\mathbf{v}_i = \mathbf{v}_{fi} + \boldsymbol{\omega}_i \times \mathbf{r}_i, \tag{3.6}$$

where \mathbf{v}_{fi} is the part determined by the given flapping rule. $\boldsymbol{\omega}_i$ is the angular speed of segment i . Hence,

$$\mathbf{L} = \sum_i m_i \mathbf{r}_i \times \mathbf{v}_{fi} + \sum_i m_i r_i^2 \boldsymbol{\omega}_i - \sum_i m_i (\mathbf{r}_i \cdot \boldsymbol{\omega}_i) \mathbf{r}_i. \tag{3.7}$$

To get the unique solution of Eq. (3.3), the sufficient and necessary condition is

$$\boldsymbol{\omega}_1 = \boldsymbol{\omega}_2 = \dots = \boldsymbol{\omega}. \tag{3.8}$$

Therefore,

$$\begin{cases} m \frac{d\mathbf{u}}{dt} = \mathbf{F}, \\ \frac{d}{dt} (\sum_i m_i \mathbf{r}_i \times \mathbf{v}_{fi}) + \frac{d}{dt} [\boldsymbol{\omega} \sum_i m_i r_i^2 - \sum_i m_i (\mathbf{r}_i \cdot \boldsymbol{\omega}_i) \mathbf{r}_i] = \mathbf{M}. \end{cases} \quad (3.9)$$

After \mathbf{u} and $\boldsymbol{\omega}$ were obtained from Eq. (3.9), the new position and attack angle of fish body can be yielded by

$$\begin{cases} \frac{d\mathbf{x}}{dt} = \mathbf{u}, \\ \frac{d\boldsymbol{\theta}}{dt} = \boldsymbol{\omega}, \end{cases} \quad (3.10)$$

where $\boldsymbol{\theta} = \theta_x \mathbf{i} + \theta_y \mathbf{j} + \theta_z \mathbf{k}$, θ_x , θ_y and θ_z are the angles of the projection of the central line of fish body on the planes of $y-z$, $z-x$ and $x-y$ to the positive directions of y , z and x axis, respectively.

3.3 The flapping rule and kinematic parameters

The motion of the 3D bionic fish consists of two parts, namely, the undulation of the body trunk and the oscillation of the tail. It is assumed that the bending of 3D fish body is fully specified by the undulation of its backbone. The undulation, which is characterized by a traveling wave, only happens within the (x_l, y_l) plane

$$y_l(x_l, t) = a(x_l) \sin(k_w x_l - \omega t), a(x_l) = c_1 x_l + c_2 x_l^2, \quad -0.3 \leq x_l \leq 0.7, \quad (3.11a)$$

$$\theta_l = \alpha \sin(k_w x_{lp} - \omega t + \psi). \quad (3.11b)$$

Where $k_w = 2\pi/\lambda$ is the wavenumber, λ is the corresponding wavelength, $\omega = 2\pi/T$ is the circular frequency corresponding to the beat period T . $x_l = 0$ is the mass centre of fish body. The front point of the caudal, attached to the peduncle, follows the path of the peduncle. At the same time, the caudal fin can undergo a pitch motion around the front point. The angle of attack θ_l with respect to the x_l -axis is defined by Eq. (3.11b). Where α is the maximum angle of attack, $x_{lp} = 0.7$ is the coordinate of the peduncle in the fish body coordinates, and ψ is the phase difference between the pith motion of the caudal fin and the undulation of the fish body. In this study, the kinematic parameters of the self-propelled swimming fish are taken as $T = 1.0$, $\lambda = 1.22$, $\alpha = 30^\circ$, $\psi = 90^\circ$, $c_1 = 0.0$, $c_2 = 0.155$.

3.4 Boundary and initial conditions

In the topology optimization process of the 3D self-propelled swimming fish, the average physical variables in one period of steadily flapping are used to evaluate swimming performance. The distance which the 3D bionic fish travels is not long. So the computational domain is $4 \times 1 \times 1$ in the topology optimization process. All boundaries of the computational domain are assumed to be no-slip boundary conditions, $u_b = v_b = w_b = 0$. Thus,

the computational region is equivalent to a flume without inflow and outflow. The initial condition is: $u = v = w = 0$. The dimensionless length of the three-dimensional bionic fish is 1. The kinematics viscosity coefficient of fluid is $\nu = 1.0 \times 10^{-6}$. Reynolds number and Strouhal number are two important non-dimensional numbers in relation to swimming of fish. Reynolds number is defined as $Re = Ul/\nu$, where U is the motion velocity of the fish, l is the length of the fish. The Strouhal number is $St = fA/U$, where f is the frequency of oscillation, A is often approximated by the lateral total excursion of the first point of the caudal fin, and U is also the motion velocity. However, for self-propelled swimming fish, Reynolds number and Strouhal number are only determined until the calculation is finished, because the speed of fish change constantly in the process of self-propelled swimming.

Immersed boundary conditions on the body surface of the fish is shown as follows. The velocity on the body boundary is $V_b = V_0 + V_r + V_f$.

- (1) Velocity V_0 arises from hydrodynamic force

$$V_0 = u_0i + v_0j + w_0k. \tag{3.12}$$

- (2) Linear velocity V_r arises from rotation

$$V_r = \omega \times (x - x_0), \tag{3.13}$$

where x is the coordinate of a point on the surface of the fish body, and x_0 is the coordinate of the center of gravity.

- (3) Velocity V_f arises from flapping.

The motion of the fish body only exists within $x_l - y_l$ plane, in the fish body coordinates. Therefore, the components w_{lf} of V_{lf} in the direction of z_l is $w_{lf} = 0$. The velocities arising from the flapping of the body trunk and the caudal fin should be considered separately. According to Eq. (3.11a), the flapping of the body trunk only occurs in the direction of y_l . In the local body coordinate system, the velocity of the fish body caused by the flapping is

$$\left\{ \begin{array}{l} u_{lf} = \begin{cases} 0, & -0.3 \leq x_l \leq 0.7, \\ -\omega_{lf}(y_l - y_{lp}), & x_l > 0.7, \end{cases} \\ v_{lf} = \begin{cases} -\omega a(x_l) \cos(k_w x_l - \omega t), & -0.3 \leq x_l \leq 0.7, \\ v_{lp} + \omega_{lf}(x_l - x_{lp}), & x_l > 0.7, \end{cases} \\ w_{lf} = 0. \end{array} \right. \tag{3.14}$$

Where the velocity of the peduncle is $v_{lp} = \dot{y}_{lp}(t) = -\omega a(x_{lp}) \cos(k_w x_{lp} - \omega t)$ and the angular velocity of the caudal fin is $\omega_{lf} = -\omega \alpha \cos(k_w x_{lp} - \omega t + \psi)$.

If the angle of attack of fish body is θ , the boundary velocity of the fish body arising from the flapping in the global coordinate system is defined by

$$\begin{cases} u_f = u_{lf} \cos(\theta) - v_{lf} \sin(\theta), \\ v_f = u_{lf} \sin(\theta) + v_{lf} \cos(\theta), \\ w_f = w_{lf}. \end{cases} \quad (3.15)$$

4 Algorithm of the topology optimization of the caudal fin of the 3D self-propelled swimming fish

The optimization method used in the present study is a algorithm to handle nonlinearly constrained minimax problems, which has good robustness [26]. The problem considered in this method is as follows. Choose the optimal values of (x_1, \dots, x_n) to

$$\begin{cases} \text{Minimize } \omega \text{ subject to} \\ |f_i - g_i(x_1, \dots, x_n)| \leq \omega, & 1 \leq i \leq m_1, \\ g_i(x_1, \dots, x_n) \leq \omega, & m_1 + 1 \leq i \leq m_2, \\ g_i(x_1, \dots, x_n) \leq 0, & m_2 + 1 \leq i \leq m_3, \end{cases} \quad (4.1)$$

where m_1, m_2, m_3 are integers satisfying $0 < m_1 < m_2 < m_3$, the f_i are given real numbers, and the g_i are given smooth functions. The detailed optimization algorithm is referred to [26]. The adaptive optimal control of unsteady separated flow with a smart body surface and the adaptive optimal control of the flapping rule of a fixed flapping plate are successfully carried out by this optimization algorithm [27, 28].

4.1 The objective functional of the topology optimization

The evaluation of swimming performances is determined by the swimming efficiency, the swimming speed and direction control. The strategy of the swing of the fish head is used for the direction control [29]. The swimming speed and the swing of the fish head are easy to calculate. However, there is no proper methods to evaluate the swimming efficiency of fish, because it is impossible to separate the thrust from the drag exerted on a swimming fish body by now.

The Froude efficiency is generally used to measure the swimming efficiency and is defined as

$$\eta_{fr} = \frac{\langle F \rangle U}{\langle P \rangle}, \quad (4.2)$$

where U is the average speed of forward swimming of fish, $\langle F \rangle$ is the time average of thrust, and $\langle P \rangle$ is the time average of power needed. Several methods are suggested for the evaluation of thrust, but these methods are not perfectly reasonable. So there has been much dispute over the thrust for self-propelled body [30]. Since the thrust of

self-propelled fish is undetermined, the total force in the forward direction is used when evaluating the Froude efficiency in the present study. Thus, the Froude efficiency is lower than the real swimming efficiency, and only is used to compare the swimming efficiency of different kind of fish in the optimization process in this study. The Froude efficiency, which are calculated using the total force, can not be used for absolute evaluation of swimming efficiency. In order to overcome the shortages of the Froude efficiency, the energy transformation efficiency can be taken in the measure of swimming efficiency [31].

$$\eta_{power} = \frac{\frac{1}{2}mU^2}{P_{out}}, \tag{4.3}$$

where m is the mass of fish, and P_{out} is the total output power of fish. Using the energy transformation efficiency can avoid the difficulty as described above, but the change of swimming efficiency with the different parameters is not as remarkable as the Froude efficiency. Therefore, the Froude efficiency is employed for the topology optimization to save computing cost, and these two efficiencies are used together to analyze swimming performance.

The output power of swimming fish is the time integral of dot product of force with the speed on the fish body [9,32]. The time average of output power of swimming fish in one period is defined by

$$P = \frac{1}{T} \int_t^{t+T} \left[\iint_{s(t)} (-pn + \mu\omega \times n) \cdot u ds \right] dt, \tag{4.4}$$

where T is the period of flapping, $S(t)$ is the outer surface of fish, n is the outward direction vector on the body surface of fish, p is the pressure of fluid flow, ω is the angular velocity, μ is the dynamics viscosity of fluid, and $u = [u, v, w]$ is the speed on the surface of fish.

The average Froude efficiency of fish in one period is defined as

$$\bar{\eta}_{Fr} = \frac{\bar{F}_x \bar{u}}{P}, \tag{4.5}$$

where $\bar{F}_x = \frac{1}{T} \int_0^T F_x dt$ is the average total force in swimming direction (the negative direction of x) in one period, $\bar{u} = \frac{1}{T} \int_t^{t+T} u dt$ is the average swimming speed in the x direction within one period.

The work of total force in swimming direction is

$$W = \int_t^{t+T} F_x u dt. \tag{4.6}$$

The control strategy of the swing of the fish head proposed by Wu is used in direction control of the 3D bionic fish [29]. The swing amplitude of the head of the fish is

$$C_h(t) = \frac{1}{2} \{ C_{\theta_c} L_c \tan(\theta(t)) + C_y [y(t) - y_0] \}, \tag{4.7}$$

where θ_c is the angle between fish body and target swimming direction, L_c is the body length used in the direction control, $y(t)$ is the ordinate of the centre of gravity of fish body, and y_0 is the ordinate of the target trajectory. C_θ and C_y are adjustment coefficients, taking values of $C_\theta = -1.5$ and $C_y = -1.0$, respectively. $C_h(t)$ can be positive or negative. The average amplitude of the head of the fish in one swimming period is

$$\bar{C} = \frac{1}{T} \int_t^{t+T} C_h(t) dt. \quad (4.8)$$

The topology optimization functional of the caudal fin of the three-dimensional bionic fish is the function of the swimming efficiency, the swimming speed and the amplitude of the fish head. The objective of the optimization study is to find the optimal geometry of the caudal fin, which can make fish swim more efficient, faster and more flexible. The objective functional of topology optimization is

$$J = \frac{\bar{\eta}_{Fr0}}{\bar{\eta}_{Fr}} + \frac{W_0}{W} + \frac{\bar{C}}{\bar{C}_0}, \quad (4.9)$$

where $\bar{\eta}_{Fr0}$ is the swimming efficiency before topology optimization, $\bar{\eta}_{Fr}$ is the swimming efficiency after topology optimization; W_0 and W are the work of total force before and after topology optimization in one swimming period, respectively; \bar{C}_0 and \bar{C} are the swing amplitude of the 3D fish head before and after topology optimization, respectively.

4.2 The parameters of topology optimization

The caudal fin is divided into 12 regions, as shown in Fig. 12. The width of each region is 2 or 3 times the minimum size of grid at the maximum number of refinement levels 7. The coefficient of water permeability of each region is the optimization parameter $coe[i]$. It is impossible that the optimal caudal fin has many small holes whose sizes are about equal to the width of computational grids. So the optimization parameter based on each mesh are not necessary. In order to save computing time, the optimization parameters $coe[i]$ chosen in the above are not the best, but feasible and efficient for the topology optimization of the caudal fin. The region, which is favorable to the swimming performance, is impermeable. Otherwise it is permeable and is removed from the tail. With

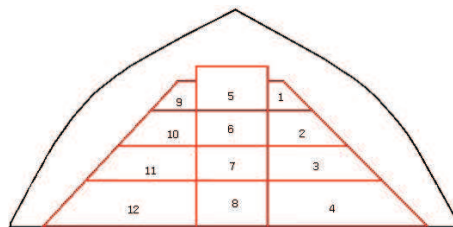


Figure 12: The partitions of caudal fin (at the central section).

the immersed boundary method, the coefficients of water permeability of all regions are applied to the 3D bionic fish body in the process of topology optimization. Provided the region of the caudal fin is permeable, the coefficients of water permeability are $coe[i]=0.0$. In the opposite, the coefficients of water permeability are $coe[i]=1.0$

4.3 The procedure of topology optimization of the caudal fin

Take the triangular caudal fin as the initial shape, as shown in Fig. 13, calculate the average swimming efficiency, average swimming speed and the swing amplitude of the head of the fish within one swimming period; Then do the topology optimization to adjust the coefficient of water permeability; Apply the optimized parameters to the CFD, until the realization of optimal functional. The pseudo-procedures of the process of the topology optimization are as follows:

```

{
  iter = 0,
  set initial  $coe_0[i]$ , call for CFD module to get the initial functional  $J_0, J_{\min} = J_0$ ;
  DO
    Call for topology optimization program to get  $coe^*[i]$ ;
    If  $coe^*[i] < 0.3$ , then  $coe^*[i] = 0.0$ ;
    Apply  $coe^*[i]$  to the 3D caudal fin and call for CFD module to calculate  $J^*$ ;
    If  $J^* \leq J_{\min}$  Then  $J_{\min} = J^*$ ;
    iter = iter + 1;
  ENDDO WHILE  $J_{\min}$  is smaller than a small number.

```

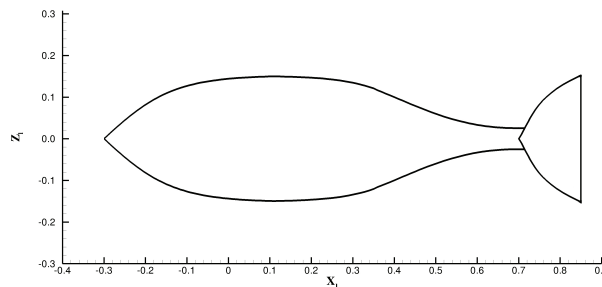


Figure 13: The body shape of the bionic fish before the optimization.

5 Results of topology optimization

5.1 The comparison of the swimming performances before and after topology optimization

According to the study of vorticity dynamics of self-propelled swimming of the three-dimensional fish [33], the contribution to the thrust by the caudal fin is gradually reduced with the increase of the swimming speed. Therefore the topology optimizations

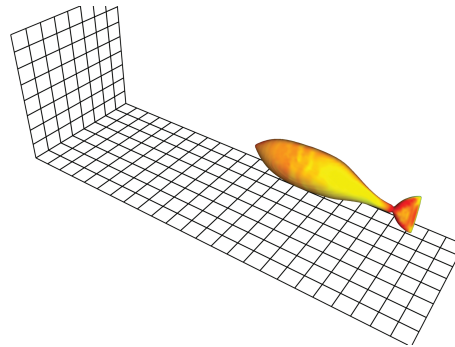


Figure 14: The geometry of the 3D bionic fish before optimization.

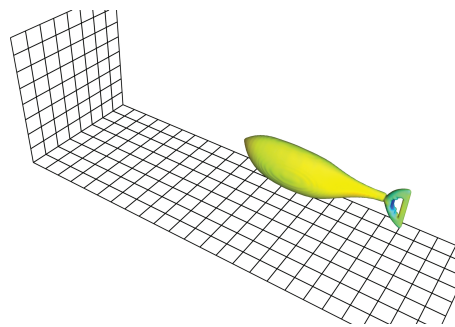


Figure 15: The geometry of the 3D topology optimized bionic fish.

of the caudal fin of the 3D bionic fish are investigated at four different types of initial swimming speeds $u = -0.1$, $u = -0.2$, $u = -0.3$, $u = -0.35$, respectively. Thus a variety of moving modes, containing the low speed swimming, the moderate speed and the high speed swimming, are considered in the present study. Corresponding to different initial swimming speeds, Reynolds number are about $Re = 1.0 \times 10^5$, $Re = 2.0 \times 10^5$, $Re = 3.0 \times 10^5$ and $Re = 3.5 \times 10^5$, respectively. The geometry of the 3D bionic fish before the topology optimization is like triangle, as shown in Fig. 14. The coefficients of water permeability before the topology optimization are $coe[i] = [1.0, 1.0, 1.0, 1.0, 1.0, 1.0, 1.0, 1.0, 1.0, 1.0, 1.0, 1.0]$. This shows that the whole tail is impermeable at this time.

It can be seen from Table 1 that except the case of initial swimming speed $u = -0.1$, the

Table 1: The coefficients of water permeability of the caudal fin after the topology optimization.

	The coefficients of water permeability after the topology optimization
$u = -0.1$	0.0 1.0 1.0 1.0 1.0 1.0 1.0 0.0 1.0 0.0 1.0 1.0 1.0
$u = -0.2$	0.0 0.0 0.0 0.0 1.0 0.0 0.0 0.0 0.0 1.0 1.0 0.0 0.0 1.0
$u = -0.3$	0.0 0.0 0.0 0.0 1.0 0.0 0.0 0.0 0.0 1.0 0.0 0.0 0.0 1.0
$u = -0.35$	0.0 0.0 0.0 0.0 1.0 0.0 0.0 0.0 0.0 1.0 0.0 0.0 0.0 1.0

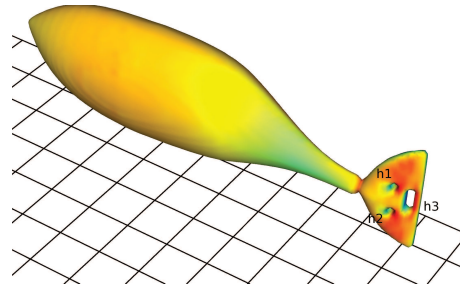


Figure 16: The geometry of the 3D bionic fish after optimization at the initial swimming speed $u = -0.1$.

permeability coefficients after topology optimizations of the other three types of swimming modes are the same. The optimal parameters form a caudal fin with three small holes at the initial swimming speed $u = -0.1$, which are $h1$, $h2$ near the leading edge of the caudal fin and $h3$ near its trailing edge, as shown in Fig. 16. The optimal caudal fin of other three types of swimming modes, as shown in Fig. 15, whose topology is different from that of the natural fish tail, is a hollow tail, and the geometry of the region near the leading edge of the caudal fin is still similar to the lunate tail. In other words, the unique optimal caudal fin, which has good swimming performance in the most of swimming states, exists. Because the larger the caudal fin area is, the faster the swimming speed of fish increase at the low swimming speed. But the proportion of propulsion contributed by the tail gradually decreases with the increase of the swimming speed. Thus, the holes of the tail fin after the topology optimization are quite small at the initial swimming speed $u = -0.1$. Table 2 shows that all swimming indicators of the optimal bionic fish of each swimming mode after 3D topology optimization are greatly improved, and especially the swimming efficiency and the swimming speed increase most significantly. Compared with the high-speed cruise, the low-speed swimming is relatively unimportant for most large fishes, such as tuna and mackerel. Therefore, through the analysis on the optimization results of the above two table, the topology optimal tail of the most swimming modes is chosen as the final geometry of the caudal fin of the 3D topology optimized bionic fish.

Table 2: The comparison of swimming performances of 3D bionic fish before and after the topology optimization.

		$\bar{\eta}_{Fr}$	W	\bar{C}	J
$u = -0.10$	before opt.	8.69%	8.68×10^{-5}	1.76×10^{-2}	3.00×10^0
	after opt.	9.30%	8.20×10^{-5}	1.49×10^{-2}	2.84×10^0
$u = -0.20$	before opt.	14.75%	1.18×10^{-4}	2.80×10^{-2}	3.00×10^0
	after opt.	22.95%	1.38×10^{-4}	2.20×10^{-2}	2.28×10^0
$u = -0.30$	before opt.	14.18%	9.90×10^{-5}	3.04×10^{-2}	3.00×10^0
	after opt.	46.62%	1.85×10^{-4}	2.00×10^{-2}	1.49×10^0
$u = -0.35$	before opt.	11.61%	7.56×10^{-5}	3.14×10^{-2}	3.00×10^0
	after opt.	57.95%	2.43×10^{-4}	2.82×10^{-2}	1.41×10^0

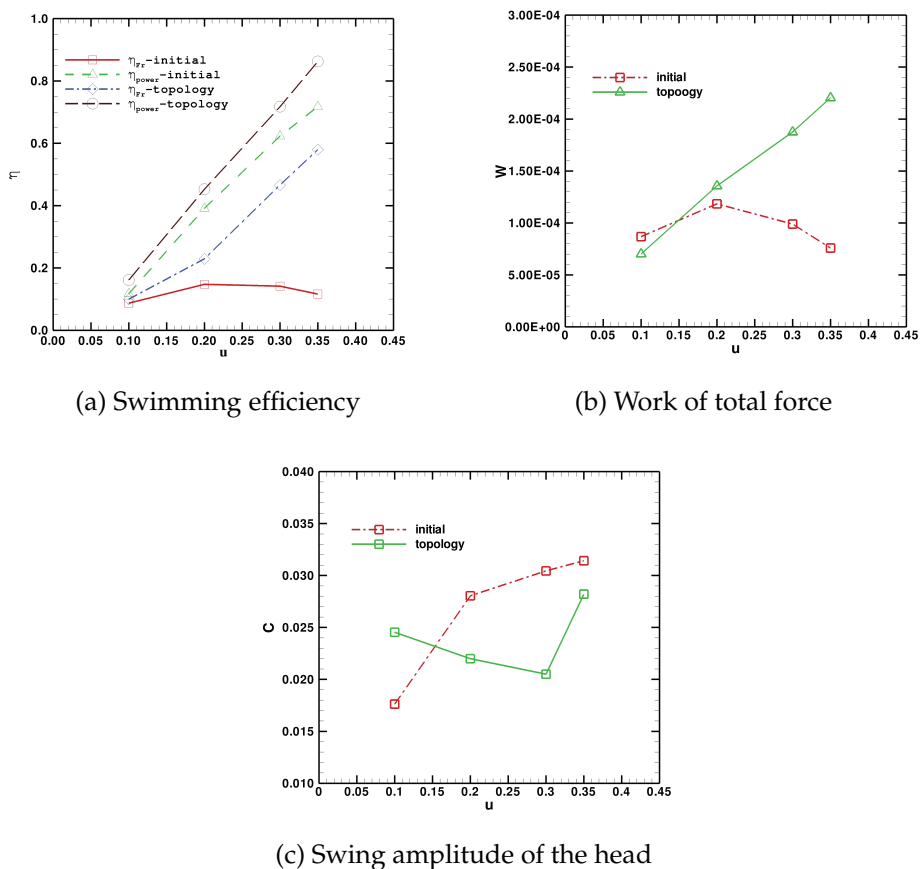


Figure 17: Comparison of the swimming performances of the initial bionic fish and the 3D topology optimized bionic fish.

The comparisons between the swimming performances of the initial bionic fish and the 3D topology optimized bionic fish in the different swimming modes, not only show that the 3D topology optimized bionic fish has higher swimming performance, but also represent the variation of the swimming performances of two types of the bionic fish with the change of swimming speed. It can be seen from Fig. 17(a) that the Froude efficiency and energy transformation efficiency of the 3D topology optimized bionic fish are obviously higher than that of the initial bionic fish, and increases rapidly with the swimming speed. By observing the Froude efficiency, it is found that the swimming efficiency of the initial bionic fish slightly increase when the swimming speed is relatively low, but its swimming efficiency begins to decline as the swimming speed exceeds a certain value. These changes can not be seen from the energy transformation efficiency. Fig. 17(b) shows that the work of total force of the 3D topology optimized bionic fish is smaller than the initial bionic fish just at the low swimming speed, but improve significantly with the increase of swimming speed. The work of total force of the initial bionic fish begins to

decrease after the swimming speed is greater than the middle speed. This is the reason why the swimming speed of the initial bionic fish increases more slowly at the middle and high swimming speed. Fig. 17(c) shows that the swing amplitude of the head of the 3D topology optimized bionic fish is smaller in most cases, except low-speed swimming. The 3D topology optimized bionic fish can swim more flexibly. In conclusion, the 3D topology optimized bionic fish achieves high swimming capabilities in a variety of swimming modes. Especially the swimming efficiency and swimming speed of the 3D topology optimized bionic fish increased significantly, compared with the initial bionic fish with the triangular caudal fin. All indexes of the swimming performance of the 3D topology optimized bionic fish improve obviously with the increase of the swimming speed. The initial bionic fish is not suitable for moderate and high-speed swimming.

5.2 The BVF analysis of self-propelled swimming of the 3D bionic fish

The previous section only describes the results of the topology optimizations and the variations of the swimming performances of the initial bionic fish and the 3D topology optimized bionic fish with the change of swimming speed.

The boundary vorticity flux (BVF) theory gives a set of total force and moment formulas to which the net contributor is the first and second vector moments of BVF, respectively. For a flow past a generic body surface, the total force and moment can be cast to proper surface integrals of the vectorial moments of vorticity generation rate from the surface, through transforming the original integrand into the moment of space derivative. Thus, it can reveal dynamic processes of integral variables and trace their underlying physical sources. Some of the original basic physical variables are expressed in the form of derivative. When these physical variables are used to analyze the flow field, the benefits and shortcomings inherent in the flow can be magnified. It can tell very intuitively not only what local peaks of BVF on the body surface are favorable (unfavorable) and should be enhanced (minimized), but also how to do [22, 23]. In this section, the distribution of boundary vorticity flux (BVF) on the fish body surface is analyzed to reveal the physical mechanism of the above results.

Due to the control of fish motion, the rotation of the 3D bionic fish occurs mainly within the $x-y$ plane. The calculating results shows that σ_{pz} is dominant in components of the BVF. Therefore, the analyses of the boundary vorticity flow are focused on σ_{pz} in the present study. It can be seen from Fig. 17(a) that at the swimming speed $u = 0.3$, the swimming efficiency of the initial bionic fish with the triangle caudal fin is still high compared with that at the low swimming speed, but obviously inferior to the swimming efficiency of the 3D topology optimized bionic fish. It is appropriate that the comparison of the BVF distribution of two types of bionic fish is carried out at the initial swimming speed $u = 0.3$.

Fig. 18 and Fig. 19 show the distribution of BVF σ_{pz} on body surface of the initial bionic fish at several moments of one flapping period. Although the BVF on the initial bionic fish body surface varies constantly in a swimming period, the common feature

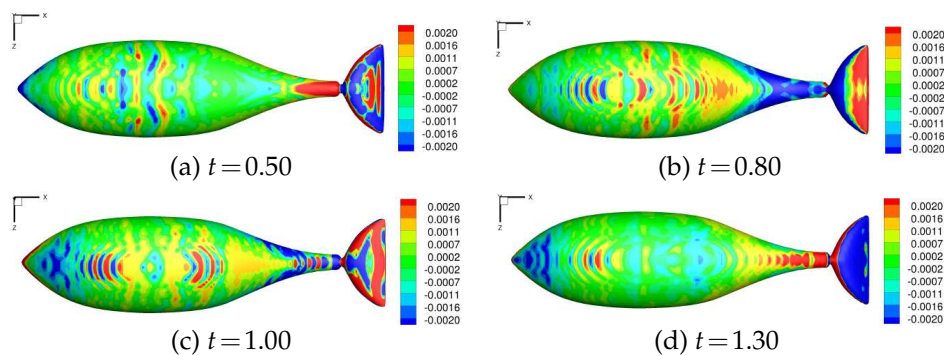


Figure 18: Contour of BVF σ_{pz} on the body surface of the initial bionic fish (top view).

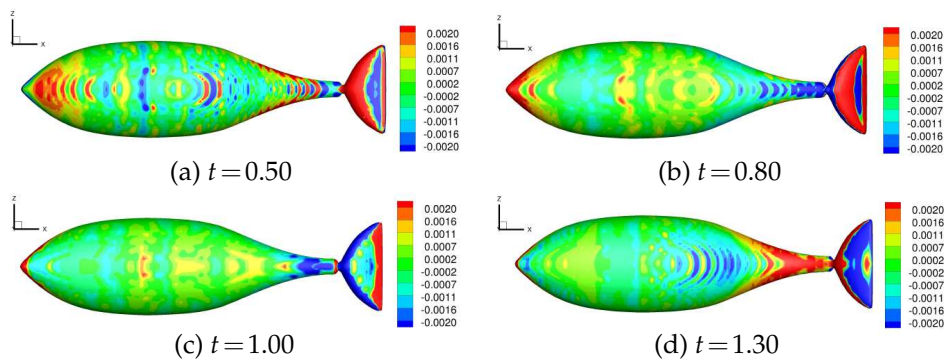


Figure 19: Contour of BVF σ_{pz} on the body surface of the initial bionic fish (bottom view).

is that the BVF distributions on the tail surface are not uniformly continuous. In most cases, the BVF in the region near the leading edge and the trailing edge is uniform, but the BVF peak zones with opposite direction occurs in the centre region of the tail surface, especially as shown in Figs. 18(a), (c) and Figs. 19(a), (b), (d). For fishes employing the body and/or caudal fin swimming (BCF), the majority of the thrust is provided by the caudal fin. Since the BVF in the centre region of the tail is opposite to the BVF in the region near the leading edge and the trailing edge, it leads to the decrease of the total vorticity generating on the tail. This is detrimental to swimming propulsion. If the centre region of the tail is removed from fish body, the total vorticity creating on the caudal fin will be greatly improved, and the thrust and the swimming efficiency will also be increased. Based on the BVF analysis, it can be found that the optimal tail is a hollow caudal fin, which is different from the nature caudal fin. The geometry of the natural fish is currently a singly connected region. Through millions of years of evolution, the natural fish do not adopt the hollow caudal fin. The main reasons may be that such a hollow caudal fin is not conducive to the blood circulation and the growth of fish body. In the nature, most fishes use a compromise solution by removing the central region and

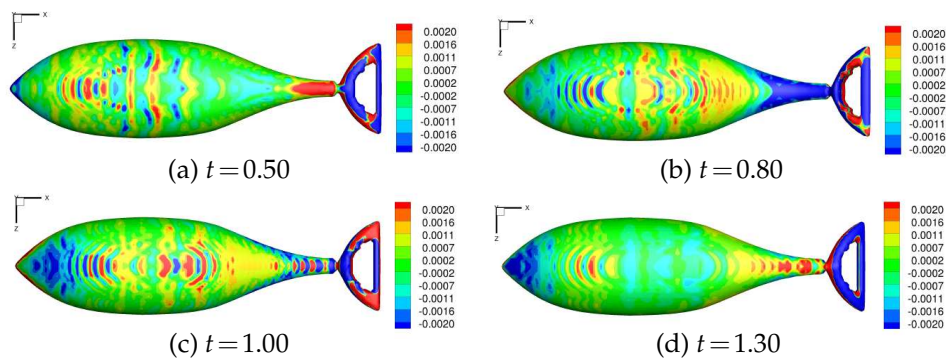


Figure 20: Contour of BVF σ_{pz} on the body surface of the 3D topology optimized bionic fish (top view).

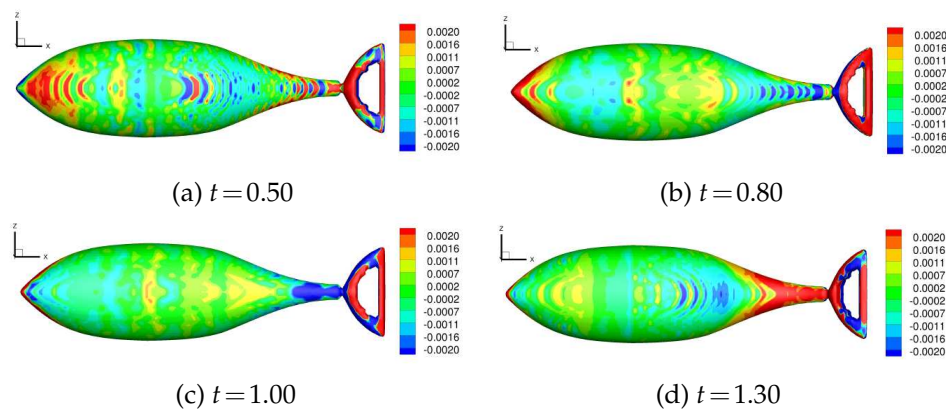


Figure 21: Contour of BVF σ_{pz} on the body surface of the 3D topology optimized bionic fish (bottom view).

the trailing edge from the triangle tail. Thus the vorticity on the unilateral surface of the caudal fin do not offset each other. But the bionic fish can use the hollow caudal fin to improve the swimming performance.

Fig. 20 and Fig. 21 represents the distribution of BVF σ_{pz} on body surface of the 3D self-propelled swimming topology optimized bionic fish at several moments of one swing period. In most cases, the BVF on each side of the caudal fin surface has the same direction and is continuous, as seen in Fig. 20(a), (d) and Fig. 21(a), (b), (c). After the topology optimization, the 3D topology optimized bionic fish just eliminates the central regions of the caudal fin of the initial bionic fish, where the BVF is opposite to the BVF in the region near the leading edge and the trailing edge of the caudal fin of the initial bionic fish. The joints of the leading and trailing edges of the caudal fin of the 3D topology optimized bionic fish appear the opposite boundary vorticity flux only in very few cases. It has little impact on the propulsion of the 3D topology optimized bionic fish. So the total strength of vorticity on the body of the 3D topology optimized bionic fish is much higher than that of the initial bionic fish. Due to the special shape of the caudal fin, the

3D topology optimized bionic fish also has stronger vorticity output than the fish with the lunate tail. The swimming performances of the 3D topology optimized bionic fish make great improvements.

6 Comparison between the topology optimized bionic fish and the fish with the lunate tail

In many studies, it is found that the fishes with the lunate tail have the highest swimming efficiency among most fishes in the nature. Through the study of the shape optimization of the caudal fin of the three-dimensional self-propelled swimming fish [34], it is shown that the lunate tail is not the optimal caudal fin of all swimming modes. The 3D bionic fish with the triangular caudal fin achieves relatively high swimming efficiency at the low swimming speed, because the larger the tail area is, the more rapidly the fish starts. The larger the caudal fin area is, the greater the resistance applied on the fish body also is at the cruise stage. At this time, the caudal fin, whose area is a little smaller than the area of the nature lunate fin, has better swimming efficiency. But the swimming efficiency of the lunate tail is the best at the close high speed, and is relatively high in a variety of other swimming modes. Therefore, the highest swimming performance of the fish with the lunate tail and the swimming performance of the 3D topology optimized bionic fish in the same fluid flow conditions, namely, the identical computing domain, the identical initial swimming speed and swing rules, are compared in this section.

6.1 Comparison of parameters related to the swimming performance

In the following discussion, the comparative analyses of the swimming performances of the fish with the lunate tail and the swimming performance of the 3D topology optimized bionic fish at the initial swimming speed $u = -0.30$ are performed. For the initial swimming speed $u = -0.30$, Strouhal number are about $St = 0.43$, and Reynolds number are about $Re = 3.0 \times 10^5$, respectively. Fig. 22(a) shows that the Froude efficiency of the 3D topology optimized bionic fish is several times the Froude efficiency of the fish with the lunate tail, and increase significantly with the increase of swimming speed. As the swimming speed increases, the fish with the lunate tail quickly soon reaches the highest Froude efficiency, then the Froude efficiency of the fish with the lunate tail declines slightly. This shows that the swimming efficiency of the fish with the lunate tail is highest at the close high speed but high-speed cruise. Because the fish with the lunate tail usually swims at high speed, and also takes into account low-speed swimming, moderate speed swimming and rapid-starts. From Fig. 22(b), it can be seen that the energy transformation efficiency of the topology optimized bionic fish is also higher than that of the fish with the lunate tail, and increase more rapidly. Compared with the energy transformation efficiency, the Froude efficiency better reflects the variation of the swimming efficiency in the different swimming modes. For all fishes, the energy transformation efficiency gradual-

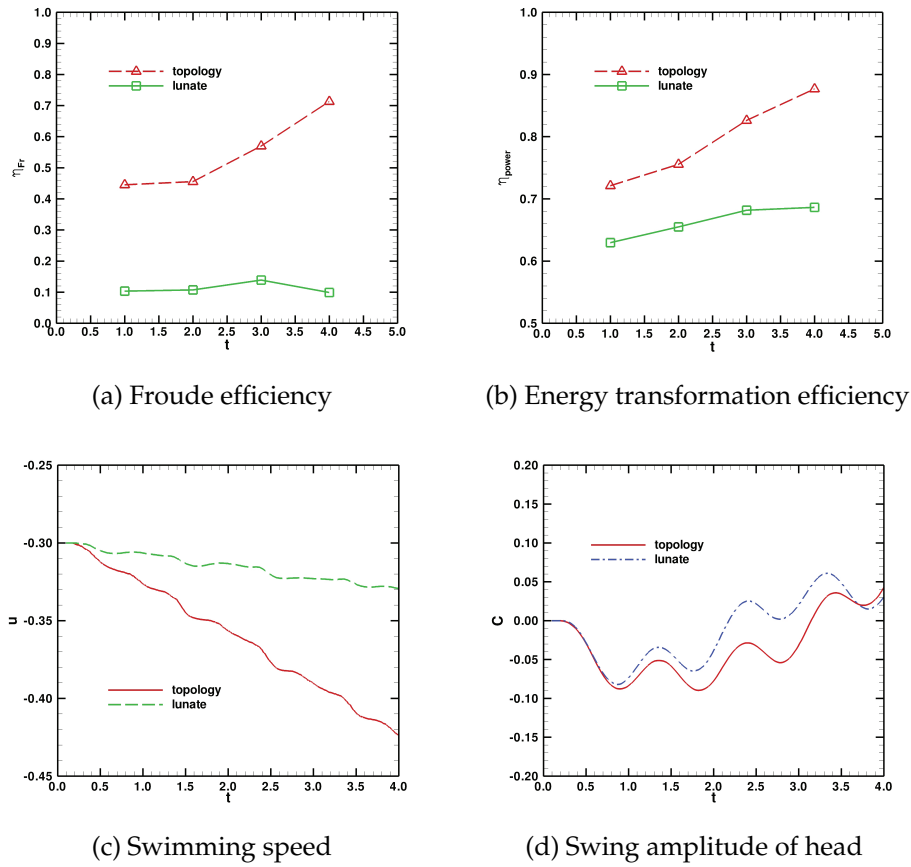


Figure 22: Comparison of the fish with the lunate tail and the 3D topology optimized bionic fish.

ly increases before the cruise stage, and keeps the maximum efficiency at the high-speed cruise. But the energy transformation efficiency can overcome the difficulty of the Froude efficiency at cruise stage, as shown in the previous discussion. It can be seen clearly from Fig. 22(c) that the swimming speed of the 3D topology optimized bionic fish increases more rapidly than the fish with the lunate tail in the identical conditions. Fig. 22(d) represents that the swing amplitude of the head of the 3D topology optimized bionic fish is almost the same as that of the fish with the lunate tail. The 3D topology optimized bionic fish not only achieves higher swimming efficiency and speed, but also swims flexible.

6.2 Comparison of the 3D vortex structures

Fig. 23(a) and Fig. 23(b) show the forces on fish body computed by the boundary vorticity flux theory. The maximum thrusts (namely the x component of total forces, F_x) of the fish with the lunate tail and the 3D topology optimized bionic fish appear at time $t = 1.5$ in the flapping cycle from $t = 1.00$ to $t = 2.00$. The comparative analyses of the fluid field

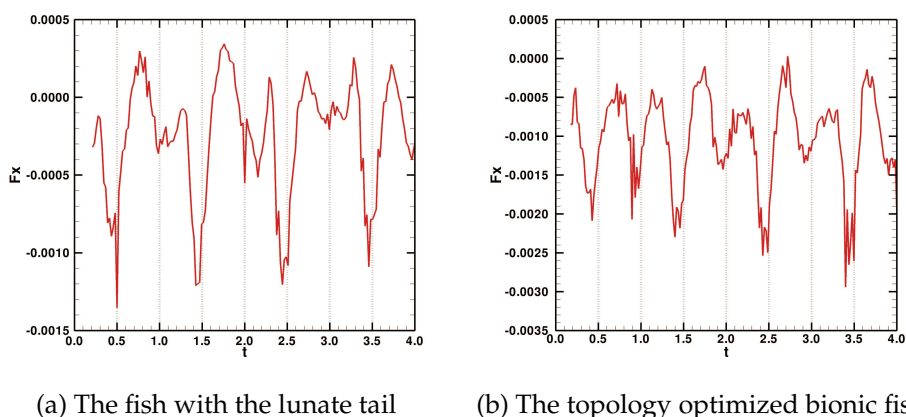


Figure 23: Comparison of the forces applied on the fish with the lunate tail and the 3D topology optimized bionic fish.

and the 3D vortex structures at the moment are carried out. The λ_2 method of Jeong and Hussain [35] is used to identify the 3D vortical structure of the 3D fish swimming in the present study. In order to analyze the evolution features of the 3D vortex structures clearly, the proper signs are marked to distinguish 3D wake structures in the figures of the 3D vortex structure of self-propelled swimming. Vortex and tip vortices attached to the caudal fin are labelled with V and TV , respectively. Vortex ring and vortex tube constituting vortex loop are denoted respectively with L and LV . The first digit of the subscripts corresponds to the different half-cycles of the fish swimming and the second digit of the subscripts indicates the different vortices or vortex loops at the same time. The arrows show the direction of vortex or vortex loops [36,37].

Due to the distinctive feature of the caudal fin of the 3D topology optimized bionic fish, it forms the nested double vortex rings attached to the caudal fin, as shown in Fig. 25(a), (b) and (c). At this moment, vortex $V31$, $TV3$ and $V32$ constitute another vortex ring while vortex $V31$ and $TV3$ form a vortex ring. Vortex ring $L11$ and $L12$ are the double vortex rings created in the preceding cycle, and vortex ring $L21$ and $L22$ are the double vortex rings produced in the preceding half cycle. The double vortex rings produced at different moments respectively locate on the top sides and bottom sides of the caudal fin. This kind of double vortex rings are never observed in the wake of the fish with the ordinary caudal fin. Only Lauder [5] found the similar double vortex ring in the wake of the shark with the heterocercal tail.

It can be seen from Fig. 24 that there are not double vortex rings in the wakes of the fish with the lunate tail, distinguished from the wakes of the 3D topology optimized bionic fish. The comparison of the forces from Fig. 23 shows that the forces F_x of the fish with the lunate tail begin to slowly decrease with the increase of swimming speed, but that of the 3D topology optimized bionic fish gradually increase under the same conditions. The reason for this difference between swimming speeds of two types of bionic fish is that the vortex rings generated by the lunate caudal fin slip off to the sides

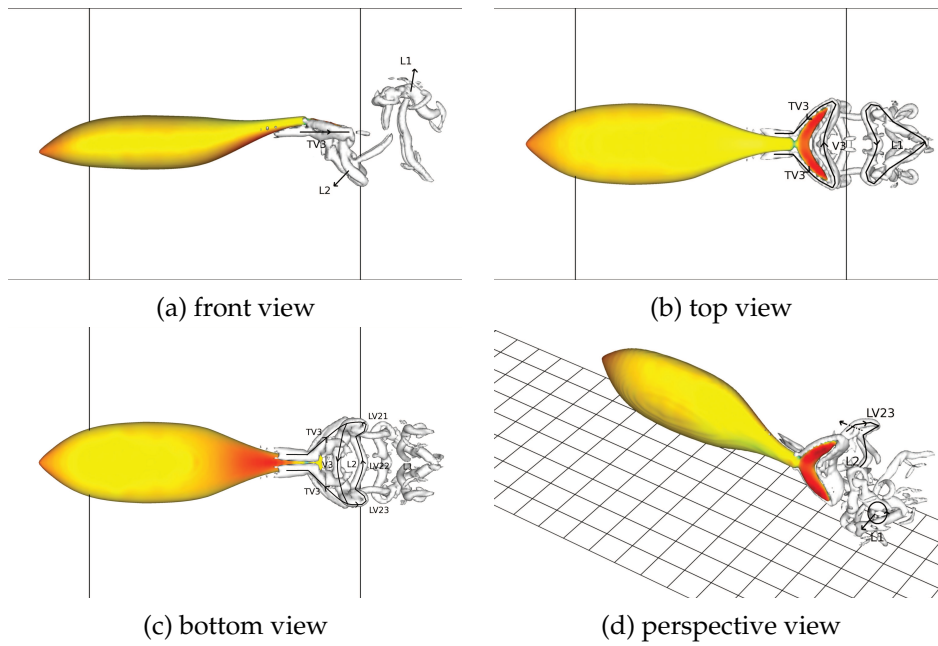


Figure 24: The 3D vortex structure of self-propelled swimming of the 3D bionic fish with the lunate tail at $t=1.50$, shown in the isosurfaces of λ_2 .

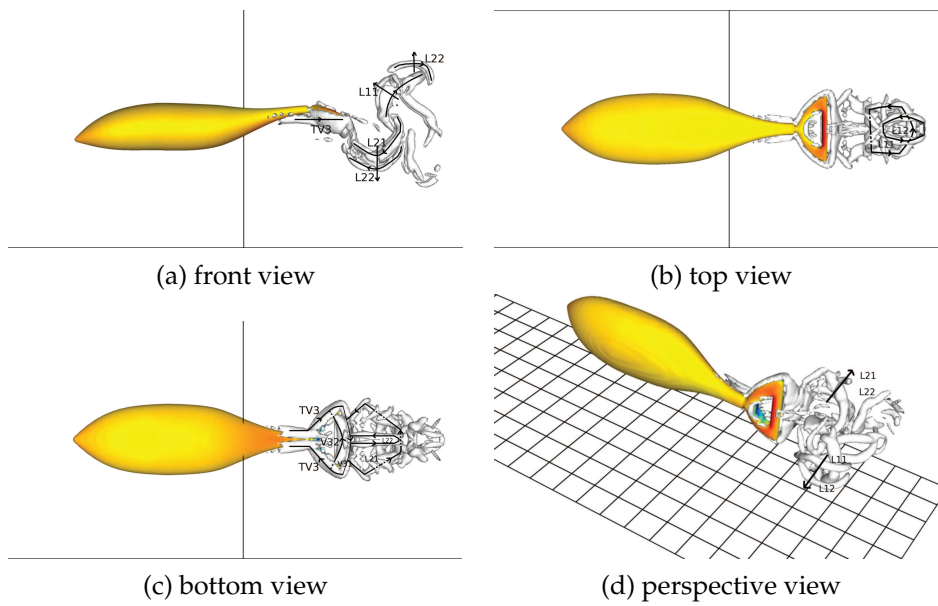


Figure 25: The 3D vortex structure of self-propelled swimming of the 3D topology optimized bionic fish at $t=1.50$, shown in the isosurfaces of λ_2 .

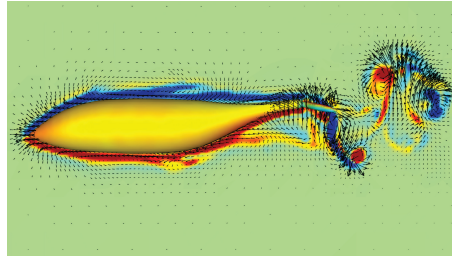


Figure 26: Flow field and contour levels of ω_z in $x-y$ slice at $t=1.50$ for the 3D bionic fish with the lunate tail.

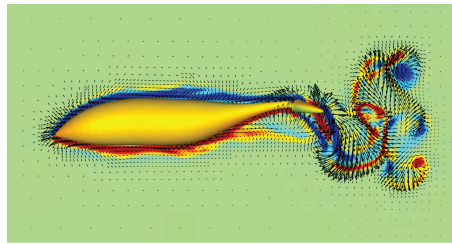


Figure 27: Flow field and contour levels of ω_z in $x-y$ slice at $t=1.50$ for the 3D topology optimized bionic fish.

of caudal fin. The directions of vortex $L21$ and $L23$, which are the components of vortex rings $L2$, formed by right-handed screw rule, is parallel to the forward direction of the fish, as shown in Fig. 24(c), (d). This is unfavorable to the propulsion. Only the vortex rings, whose directions determined by the right-handed screw rule is not parallel to the forward direction, can contribute to propulsion as the vortex ring $L1$. As the swimming speed continues to increase, vortex $L21$ and $L23$ gradually become clear, but the vortex $L22$ slowly disappears. Thus there are not vortex rings, which obviously contribute to propulsion, in the wake of the fish with the lunate tail. This is the reason why the cruise speed of the fish with the lunate tail is relatively lower than the 3D topology optimized bionic fish. By comparing Figs. 24(a) with Fig. 25(a), the strength of the vortex induced by the 3D topology optimized bionic fish is much higher than that of the fish with the lunate tail. For the 3D topology optimized bionic fish, vortex rings shed successively in a swing cycle interconnect, but a set of vortex contrails connect two adjacent vortex loops in the wake of the fish with the lunate tail, as seen in Fig. 24(a) and Fig. 24(d). Thus the flow field induced by the vortex rings in the wake of the 3D topology optimized bionic fish makes significant improvement. It can be seen from Fig. 26 and Fig. 27 that the micro-jet in the wake of 3D bionic fish with topology optimized caudal fin is much stronger than that of lunate caudal fin. The stronger the jet is, the greater the thrust is. Thus the 3D topology optimized bionic fish has higher swimming performances than the fish with the lunate tail.

7 Conclusions

Topology optimization of the caudal fin of the three-dimensional self-propelled swimming fish show that the optimal caudal fin of all kinds of swimming modes is basically the same. The topology optimization caudal fin, whose topology is different from that of the natural fish tail, is a hollow caudal fin, and the geometry of the region near the leading edge of the caudal fin is still similar to the lunate caudal fin. The 3D topology optimized bionic fish has high swimming performances in a variety of swimming modes. In particular, the swimming efficiency and the swimming speed of the 3D topology optimized bionic fish increased obviously, compared with the initial bionic fish before topology optimization. All indexes of the swimming capability of the 3D topology optimized bionic fish improve significantly with the increase of the swimming speed. The initial bionic fish with the triangular caudal fin is not suitable for moderate and high-speed swimming. The distributions of the boundary vorticity flux on the triangular caudal fin surface before the topology optimization are not uniformly continuous, and the most obvious feature is that the BVF peak zones with opposite direction occurs in the centre region of the triangular tail surface, but the BVF in the region near the leading edge and the trailing edge is uniform. The 3D topology optimized bionic fish just eliminates the central regions of the triangular caudal fin before topology optimization, thus the total strength of vorticity on the body of the 3D topology optimized bionic fish is much higher than that of the initial bionic fish. Due to the special geometry of the caudal fin, the 3D topology optimized bionic fish also has stronger vorticity output than the fish with the lunate tail having the highest swimming efficiency in the natural world. The micro-jet induced by the double vortex rings in the wake of the 3D bionic topology optimized fish is much stronger than that of the bionic fish with the lunate tail. In short, the 3D bionic topology optimized fish has many advantages. The area of the topology optimized tail is larger than the lunate tail, the hollow structural characteristic reduces the adverse effect on propulsion at the high swimming speed, and the 3D bionic topology optimized fish controls the swimming direction more easier. The swimming performances of the 3D topology optimized bionic fish make great improvements.

Acknowledgments

The authors acknowledge the support of National Natural Science Foundation of China (Grant No. 11302071) and National Postdoctoral Foundation of China (Grant No. 2013M541597). Our deep appreciation goes to Professor Wei SHYY of Hong Kong University of Science and Technology, for detailed discussion and kindly help.

References

- [1] J. GRAY, *Studies in animal locomotion: Roman 6. The propulsive powers of the dolphin*, J. Exp.

- Biol., 13 (1936), pp. 192–199.
- [2] T. Y. WU, *Fish swimming and bird/insect flight*, Annu. Rev. Fluid Mech., 43 (2011), pp. 25–58.
 - [3] J. Y. CHENG, L. X. ZHUANG, AND B. G. TONG, *Analysis of swimming 3-D waving plate*, J. Fluid. Mech., 232 (1991), pp. 341–355.
 - [4] F. CANDELIER, F. BOYER, AND A. LEROYER, *Three-dimensional extension of Lighthill's large-amplitude elongated-body theory of fish locomotion*, J. Fluid. Mech., 674 (2011), pp. 196–226.
 - [5] F. E. FISH AND G. V. LAUDER, *Passive and active flow control by swimming fishes and mammals*, Annu. Rev. Fluid Mech., 38 (2006), pp. 193–224.
 - [6] E. D. TYTELL AND G. V. LAUDER, *The hydrodynamics of eel swimming, Roman 1. Wake structure*, J. Exp. Biol., 207 (2004), pp. 1825–1841.
 - [7] M. S. TRIANTAFYLLOU, G. S. TRIANTAFYLLOU AND D. K. P. YUE, *Hydrodynamics of fishlike of swimming*, Annu. Rev. Fluid Mech., 32 (2000), pp. 33–53.
 - [8] Q. ZHU, M. J. WOLFGANG, D. K. P. YUE AND M. S. TRAIANTAFYLLOU, *Three-dimensional flow structures and vorticity control in fish-like swimming*, J. Fluid. Mech., 468 (2002), pp. 1–28.
 - [9] H. LIU AND K. KAWACHI, *A numerical study of undulatory swimming*, J. Comput. Phys., 155 (1999), pp. 223–247.
 - [10] C. J. WU AND L. WANG, *Numerical simulations of self-propelled swimming of 3D bionic fish school*, Sci. China, 52(3) (2009), pp. 658–669.
 - [11] M. SFAKIOTAKIS, D. M. LANE, AND J. B. C. DAVIES, *Review of fish swimming modes for aquatic locomotion*, IEEE J. Oceanic. Eng., 24(2) (1999), pp. 237–252.
 - [12] G. V. LAUDER, *Function of the caudal fin during locomotion in fishes: kinematics, flow visualization, and evolutionary patterns*, Amer. Zool., 40(1) (2000), pp. 101–122.
 - [13] G. V. LAUDER AND J. C. NAUEN, *Hydrodynamics of caudal fin locomotion by chub mackerel, Scomber japonicus*, J. Exp. Biol., 205 (2002), pp. 1709–1724.
 - [14] S. HEO, T. WIGUNA, H. C. PARK AND N. S. GOO, *Effect of an artificial caudal fin on the performance of a biomimetic fish robot propelled by piezoelectric actuators*, J. Bionic. Eng., 4 (2007), pp. 151–158.
 - [15] X. ZHANG, Y. M. SU, AND Z. L. WANG, *Numerical and experimental studies of influence of the caudal fin shape on the propulsion performance of a flapping caudal fin*, J. Hydrodyn., 23(3) (2011), pp. 325–332.
 - [16] M. P. BENDSØE AND O. SIGMUND, *Topology Optimization: Theory, Methods and Applications*, Springer-Verlag, Berlin, Germany, 2003.
 - [17] T. BORRVALL AND J. PETERSSON, *Topology optimization of fluids in Stokes flow*, J. Numer. Methods Fluids., 41(1) (2003), pp. 77–107.
 - [18] J. K. GUEST AND J. H. PRÉVOST, *Topology optimization of creeping fluid flows using a Darcy-Stokes finite element*, Int. J. Numer. Meth. Eng., 66, (2006), pp. 461–484.
 - [19] L. H. OLESEN, F. OKKELS AND H. BRUUS, *A high-level programming-language implementation of topology optimization applied to steady-state Navier-Stokes flow*, Int. J. Numer. Meth. Eng., 69 (2006), pp. 975–1001.
 - [20] S. W. ZHOU AND Q. LI, *A variational level set method for the topology optimization of steady-state Navier-Stokes flow*, J. Comput. Phys., 227 (2008), pp. 10178–10195.
 - [21] X. B. DUAN, Y. C. MA AND R. ZHANG, *Shape-topology optimization for Navier-Stokes problem using variational level set method*, J. Comput. Appl. Math., 222 (2008), pp. 487–499.
 - [22] J. Z. WU, H. Y. MA AND M. D. ZHOU, *Vorticity and Vortex Dynamics*, Springer-Verlag, Berlin, Germany, 2006.
 - [23] J. Z. WU, X. Y. LU AND L. X. ZHANG, *Integral force acting on a body due to local flow structures*, J. Fluid. Mech., 576 (2007), pp. 265–286.

- [24] A. T. JOHNSON, AND V. C. PATEL, *Flow past a sphere up to a Reynolds number of 300*, J. Fluid. Mech., 378 (1999), pp. 19–70.
- [25] J. M. ANDERSON, K. STREITLIEN, D. S. BARRETT, AND M. S. TRIANTAFYLLOU, *Oscillating foils of high propulsive efficiency*, J. Fluid Mech., 360 (1998), pp. 41–72.
- [26] E. K. KAUFMAN D. J. LEEMING AND G. D. TAYLOR, *An ODE-based approach to nonlinearly constrained minimax problems*, Numer. Algorithms, 9 (1995), pp. 25–37.
- [27] L. WANG AND C. J. WU, *Adaptive optimal control of unsteady seperated flow with a smart body surface*, China J. Theory. Appl. Mech., 37(6) (2005), pp. 764–768.
- [28] C. J. WU AND L. WANG, *Adaptive optimal control of the flapping rule of a fixed flapping plate*, Adv. Appl. Math. Mech., 1(3) (2009), pp. 402–414.
- [29] C. J. WU AND L. WANG, *Where is the rudder of a fish?: the mechanism of swimming and control of self-propelled fish school*, Acta Mech. Sin., 26(1) (2009), pp. 45–65.
- [30] L. WANG, *Numerical Simulation and Control of Self-Propelled Swimming of Bionics Fish School*, PhD thesis, Hohai university, Nanjing, 2009.
- [31] S. KERN AND P. KOUMOUTSAKOS, *Simulations of optimized anguilliform swimming*, J. Exp. Biol., 209 (2006), pp. 4841–4857.
- [32] L. GUGLIELMINI AND P. BLONDEAUX, *Propulsive efficiency of oscillating foils*, Euro. J. Mech. B/Fluids, 23 (2004), pp. 255–278.
- [33] Z. Q. XIN AND C. J. WU, *Numerical simulations and vorticity dynamics of self-propelled swimming of 3D bionic fish*, Sci. China-Phys. Mech. Astron., 55(2) (2012), pp. 272–283.
- [34] Z. Q. XIN AND C. J. WU, *Shape optimization of the caudal fin of the three-dimensional self-propelled swimming fish*, Sci. China-Phys. Mech. Astron., 56(2) (2012), pp. 328–339.
- [35] J. JEONG AND F. HUSSAIN, *On the identification of a vortex*, J. Fluid Mech., 285 (1995), pp. 69–94.
- [36] K. D. VON ELLENRIEDER, K. PARKER AND J. SORIA, *Flow structures behind a heaving and pitching finite-span wing*, J. Fluid. Mech., 490 (2003), pp. 129–138.
- [37] H. DONG, R. MITTAL AND F. M. NAJJAR, *Wake topology and hydrodynamic performance of low-aspect-ratio flapping foils*, J. Fluid. Mech., 566 (2006), pp. 309–343.